RSC Advances

ROYAL SOCIETY OF CHEMISTRY

PAPER

View Article Online
View Journal | View Issue

Check for updates

Cite this: RSC Adv., 2025, 15, 32906

Structure–property relationships in tris(2-amino-5-methylpyridinium) hexabromobismuthate monohydrate with a focus on optical and electrical behavior for optoelectronics applications

Rima Altalib,[a] Imen Ibrahmi,*[a] Arafet Ghoudi,[a] Sami Znaidia,[b] Walid Rekik,[c] Jerome Lhoste[d] and Abderrazek Oueslati[a]

The hybrid compound $(C_6H_9N_2)_3[BiBr_6]H_2O$ was synthesized *via* slow evaporation and structurally characterized using single-crystal X-ray diffraction. It crystallizes in the monoclinic *C*2/*c* space group and adopts a zero-dimensional architecture composed of isolated $[BiBr_6]^{3-}$ octahedra, protonated organic cations $(C_6H_9N_2)^+$, and water molecules. These components are interconnected through hydrogen bonding and π–π interactions. Optical absorption measurements reveal a direct band gap of 2.81 eV, confirming the semiconducting nature of the material. Impedance spectroscopy, performed over a frequency range of 0.4 Hz to 3 MHz and a temperature range of 318 K to 363 K, reveals separate contributions from grains and grain boundaries. These were modeled using an equivalent circuit, indicating non-Debye relaxation behavior. The DC conductivity follows an Arrhenius-type behavior with activation energies of 0.96 and 0.51 eV. AC conductivity obeys Jonscher's power law, and the temperature-dependent decrease in the frequency exponent (*s*) supports the correlated barrier hopping (CBH) mechanism. The material exhibits enhanced dielectric permittivity, suggesting promising potential for optoelectronic and energy storage applications.

Received 10th June 2025
Accepted 26th August 2025

DOI: 10.1039/d5ra04097c

rsc.li/rsc-advances

1 Introduction

Metal halides have attracted considerable attention due to their diverse physical and chemical properties, which enable the integration of multiple functionalities within a single material system.[1–3] This versatility has fueled intense research into materials with potential applications across a wide range of technological domains. In particular, hybrid materials based on trivalent metal halides, especially those incorporating bismuth, have emerged as promising candidates for applications in nonlinear optics,[4,5] semiconductors,[6,7] ferroelectric transitions,[7] energy storage,[8,9] luminescence,[10] and thermochromism.[11]

Bismuth(III) halide complexes coordinated with organic cations exhibit remarkable structural diversity. Halobismuthate(III) compounds typically consist of anionic sublattices formed by $[BiX_6]^{3-}$ octahedra (X = halogen), which can adopt various connectivity modes such as corner-sharing, edge-sharing, or face-sharing. These arrangements give rise to a variety of dimensionalities, including discrete zero-dimensional (0D) units, one-dimensional (1D) chains, and two-dimensional (2D) layered frameworks.[12] The resulting crystal packing is stabilized by a combination of hydrogen bonding, van der Waals forces, electrostatic interactions, and halide–halide contacts.[13] Importantly, the choice of organic cation not only influences the structural organization but also plays a pivotal role in modulating the material's electronic and dielectric properties.

Aromatic amine-derived cations, such as substituted pyridinium and imidazolium species, offer distinct advantages over their aliphatic counterparts. Their relatively high dielectric constants reduce dielectric confinement, leading to lower exciton binding energies. Moreover, their π-conjugated and rigid structures facilitate stronger π–π stacking and hydrogen bonding interactions, enhancing structural stability, charge transport, and dielectric screening—critical factors for optoelectronic performance in layered halide systems.[14–19]

Several hybrid halobismuthate(III) materials incorporating aromatic amines have been reported, showing encouraging characteristics for optoelectronic applications. Examples include $(C_9H_{12}N_4)_2[BiBr_6]Cl_4H_2O$,[10] $[C_{13}H_{16}N_2]_5(BiCl_6)_3Cl$,[20]

[a]Laboratory of Spectroscopic Characterization and Optical Materials, Faculty of Sciences, University of Sfax, BP 1171, 3000 Sfax, Tunisia. E-mail: arafetghoudi199@gmail.com

[b]Laboratoire de recherche (LR 18ES19), Synthese Asymetrique et Ingenierie Moleculaire de Materiaux Organiques our L'electroniques Organiques, Facult des sciences de Monastir, 5000, Tunisia

[c]Laboratory Physical-Chemistry of Solid State, Chemistry Department, Faculty of Sciences of Sfax, University of Sfax, BP 1171, 3000, Sfax, Tunisia

[d]Institut des Molécules et Matériaux du Mans (IMMM) – UMR-6283 CNRS, Le Mans Université, Avenue Olivier Messiaen, F-72085 Le Mans Cedex 9, France

$(C_6H_{20}N_3)BiI_6H_2O$,[21] and $[C_4H_{10}N]_3[BiCl_6]$,[22] all of which demonstrate good environmental stability and functional potential. Notably, M. Hamdi *et al.*[23] reported a novel organic–inorganic hybrid material $[C_6H_{10}N_2]_7[Bi_2Cl_{11}]_2\cdot 4[Cl]$, exhibiting a dielectric constant exceeding 10^4 at 423 K. This breakthrough has further heightened interest in such materials for advanced applications.

Within this promising field of research, we report the synthesis and characterization of a new hybrid compound $(C_6H_9N_2)_3[BiBr_6]\cdot H_2O$, composed of aromatic organic molecules as the organic component, with bismuth(III) bromide as the inorganic counterpart. To elucidate its structural and physicochemical properties, a range of experimental techniques has been employed, including single-crystal X-ray diffraction, UV-visible spectroscopy, and impedance spectroscopy. The results provide valuable insight into the compound's charge transport behavior, luminescent behavior, and charge transport mechanisms. These findings contribute to the rational design of environmentally benign, lead-free hybrid materials with strong potential for optoelectronic and energy-related applications.

2 Experimental details

2.1. Synthesis of $(C_6H_9N_2)_3[BiBr_6]\cdot H_2O$

The organic–inorganic hybrid compound $(C_6H_9N_2)_3[BiBr_6]\cdot H_2O$ was synthesized *via* a slow evaporation method at room temperature. Initially, bismuth tribromide ($BiBr_3$) was dissolved in an excess of concentrated hydrobromic acid (HBr) to ensure complete dissolution. Subsequently, 2-amino-5-picoline ($C_9H_8N_2$) was added to the solution in a stoichiometric ratio of 3 : 1 with respect to $BiBr_3$, in accordance with the target compound's chemical formula. The resulting mixture was left to evaporate slowly under ambient conditions. After several days, yellow single crystals of $(C_6H_9N_2)_3[BiBr_6]\cdot H_2O$ were obtained.

$$3(C_6H_8N_2) + BiBr_3 + 3HBr + H_2O \rightarrow (C_6H_9N_2)_3[BiBr_6]\cdot H_2O \quad (1)$$

2.2. Single-crystal diffraction data collection and structure determination

A high-quality single crystal of $(C_6H_9N_2)_3[BiBr_6]\cdot H_2O$ was carefully selected using a polarizing microscope, subsequently glued and mounted at 293 K on a four-circle BRUKER APEX II area-detector diffractometer. Reflection data were acquired using graphite-monochromated Kα(Mo) radiation ($\lambda = 0.71073$ Å). All intensity data were collected using the APEX 2 program.[24] Empirical absorption corrections of the multi-scan type were applied using the SADABS program.[25] The crystal structure, belonging to the centrosymmetric space group *C*2/*c*, was solved *via* direct methods using the ShelxT-2018 software package,[26] integrated into the WINGX interface.[27] Anisotropic refinement was performed for all non-hydrogen atoms, while hydrogen atom positions were geometrically generated using the HFIX instruction included in SHELXL-2014,[26] and allowed to ride on their parent atoms. Final refinement yielded very good reliability factors: $R_1 = 0.0400$ and $wR_2 = 0.0769$. Crystal structure depictions were generated using Diamond3.2 software.[28] Detailed crystallographic data, results of the least-squares structure refinement, fractional atomic coordinates, and equivalent isotropic temperature factors are presented in Tables 1 and S1, respectively. Tables 2 and S2 provide selected bond distances, angles, and hydrogen bonds.

CCDC 2371583 contains supplementary crystallographic data for $(C_6H_9N_2)_3[BiBr_6]\cdot H_2O$. These data can be obtained free of charge from the Cambridge Crystallographic Data Center *via* https://www.ccdc.cam.ac.uk/data_request/cif.

2.3. Spectroscopy (UV-visible and complex impedance) analyses

The UV-vis absorption spectrum of the powdered sample was recorded using a Shimadzu UV-3101PC spectrophotometer.

For electrical characterization, the powder obtained from ground crystals was compressed into a pellet (8 mm in diameter and 1.1 mm thick) using a uniaxial hydraulic press under a pressure of 3500 tons per cm^2. Thin silver layers, a few nanometers thick, were manually applied to both flat surfaces of the pellet. The prepared pellet was then positioned between two platinum electrodes to perform electrical measurements. Complex impedance spectra were collected across a wide frequency range [$0.4–3 \times 10^6$ Hz] and at different temperatures [318–363 K] using a Solartron 1260 frequency response analyzer.

Table 1 Crystallographic data and structure refinements of $(C_6H_9N_2)_3[BiBr_6]\cdot H_2O$

Formula	$(C_6H_9N_2)_3[BiBr_6]\cdot H_2O$
Color/shape	Yellow/prism
Formula weight (g mol^{-1})	1033.91
Crystal system	Monoclinic
Space group	*C*2/*c*
Density	2.285
Crystal size (mm)	0.22 × 0.18 × 0.14
Temperature (K)	296(2)
Diffractometer	Bruker APEXII
a (Å)	25.208(4)
b (Å)	12.9804(13)
c (Å)	19.878(2)
β (°)	112.470(4)
V ($Å^3$)	6010.3(13)
Z	8
Radiation type	Mo Kα (0.71073 Å)
Absorption correction	Multi-scan
θ range for data collection (°)	$1.748 \leq \theta \leq 27.514$
Measured reflections	53 296
Independent reflections	6904
Observed data [$I > 2\sigma(I)$]	4527
Index ranges	$h = -32 \rightarrow 32$ $k = -16 \rightarrow 16$ $l = -25 \rightarrow 25$
F(000)	3840
Number of parameters	297
R_1	0.0400
wR_2	0.0769
Goof	1.018

Table 2 Selected bond distances (Å) and angles (°)[a]

$BiBr_6$ octahedra		Organic moieties	
Bi1–Br3	2.7537(10)	C5–C1	1.489(11)
Bi1–Br1	2.8341(7)	N2–C6	1.327(9)
Bi1–Br1$^{\mathrm{I}}$	2.8342(7)	C1–C4	1.330(10)
Bi1–Br2$^{\mathrm{I}}$	2.8472(7)	C1–C2	1.393(10)
Bi1–Br2	2.8473(7)	C2–C3	1.353(10)
Bi1–Br4	2.9841(11)	C3–C6	1.383(10)
Bi2–Br5$^{\mathrm{II}}$	2.8474(7)	C4–N11	1.347(9)
Bi2–Br5	2.8475(7)	N11–C6	1.328(9)
Bi2–Br7$^{\mathrm{II}}$	2.8534(7)	C7–C10	1.342(8)
Bi2–Br7	2.8534(7)	C7–C9	1.395(8)
Bi2–Br6	2.8559(7)	C7–C8	1.506(8)
Bi2–Br6$^{\mathrm{II}}$	2.8559(7)	N10–C12	1.346(8)
Br3–Bi1–Br1	90.681(16)	N10–C10	1.357(8)
Br3–Bi1–Br1$^{\mathrm{I}}$	90.681(16)	C9–C11	1.366(8)
Br1–Bi1–Br1$^{\mathrm{I}}$	178.64(3)	C11–C12	1.404(8)
Br3–Bi1–Br2$^{\mathrm{I}}$	88.043(17)	C12–N4	1.324(8)
Br1–Bi1–Br2$^{\mathrm{I}}$	90.65(3)	C14–C13	1.308(11)
Br1$^{\mathrm{I}}$–Bi1–Br2$^{\mathrm{I}}$	89.40(2)	C14–N9	1.328(11)
Br3–Bi1–Br2	88.043(17)	N9–C18	1.289(18)
Br1–Bi1–Br2	89.40(3)	C13–C17	1.360(9)
Br1–Bi1–Br2$^{\mathrm{I}}$	90.65(3)	C13–C15	1.528(13)
Br2–Bi1–Br2$^{\mathrm{I}}$	176.09(3)	N–C18	1.374(19)
Br3–Bi1–Br4	180.0	C18–C16	1.340(10)
Br1–Bi1–Br4	89.319(16)	C16–C17	1.33(3)
Br1–Bi1–Br4$^{\mathrm{I}}$	89.319(16)	C4–C1–C2	115.2(8)
Br2–Bi1–Br4$^{\mathrm{I}}$	91.957(17)	C4–C1–C5	122.2(8)
Br2–Bi1–Br4	91.957(17)	C2–C1–C5	122.5(7)
Br5–Bi2–Br5$^{\mathrm{II}}$	180.0	C3–C2–C1	122.2(7)
Br5$^{\mathrm{II}}$–Bi2–Br7$^{\mathrm{II}}$	93.31(2)	C2–C3–C6	120.3(8)
Br5–Bi2–Br7$^{\mathrm{II}}$	86.69(2)	C1–C4–N11	122.6(7)
Br5$^{\mathrm{II}}$-Bi2-Br7	86.69(2)	C6–N11–C4	123.3(7)
Br5–Bi2–Br7	93.31(2)	N2–C6–N11	120.3(8)
Br7–Bi2–Br7$^{\mathrm{II}}$	180.0	N2–C6–C3	123.4(8)
Br5–Bi2–Br6$^{\mathrm{II}}$	90.96(2)	N11–C6–C3	116.3(8)
Br5–Bi2–Br6	89.04(2)	C10–C7–C9	117.2(6)
Br7–Bi2–Br6$^{\mathrm{II}}$	92.54(2)	C10–C7–C8	122.3(6)
Br7–Bi2–Br6	87.456(19)	C9–C7–C8	120.6(6)
Br5$^{\mathrm{II}}$–Bi2–Br6$^{\mathrm{II}}$	89.04(2)	C12–N10–C10	123.7(5)
Br5$^{\mathrm{II}}$–Bi2–Br6	90.96(2)	C11–C9–C7	122.0(6)
Br7$^{\mathrm{II}}$–Bi2–Br6$^{\mathrm{II}}$	87.458(19)	C7–C10–N10	121.0(6)
Br7$^{\mathrm{II}}$–Bi2–Br6	92.54(2)	C9–C11–C12	119.3(6)
Br6–Bi2–Br6$^{\mathrm{II}}$	180.0	N4–C12–N10	119.5(6)
		N4–C12–C11	123.8(7)
		N10–C12–C11	116.7(6)
		C13–C14–N9	121.8(9)
		C18–N9–C14	120.9(12)
		C14–C13–C17	116.1(10)
		C14–C13–C15	120.2(12)
		C17–C13–C15	123.7(13)
		N9–C18–C16	121.0(17)
		N9–C18–N	117(2)
		C16–C18–N	122(3)
		C17–C16–C18	116.9(19)
		C16–C17–C13	123.1(16)

[a] Symmetry codes: $^{\mathrm{I}}$ $1 - x, y, 1/2 - z$: $^{\mathrm{II}}$ $3/2 - x, 1/2 - y, 1 - z$.

3 Results and discussion

3.1. Structure description

In a previous study, we reported the synthesis and characterization of a hybrid material incorporating 2-amino-5-picoline as the organic component, antimony as the metallic center, and bromine as the halogen. The resulting compound, $(C_6H_9N_2)_2[SbBr_4]Br$, crystallizes in the monoclinic $C2/m$ space group with the following unit cell parameters: a = 13.5810(10) Å, b = 19.3518(15) Å, c = 8.7980(6) Å, β = 114.820(2)°, V = 2098.7(3) Å^3, and Z = 4.[29]

In the present work, a complete substitution of Sb^{3+} by Bi^{3+} leads to a new compound with a distinct chemical formula and crystal structure. Specifically, the combination of 2-amino-5-picoline with bismuth tribromide yielded a novel organic–inorganic hybrid material, $(C_6H_9N_2)_3[BiBr_6]\cdot H_2O$. This compound crystallizes in the monoclinic system, centrosymmetric space group $C2/c$, with unit cell parameters: a = 25.208(4) Å, b = 12.9804(13) Å, c = 19.878(2) Å, β = 112.470(4)°, and V = 6010.3(13) Å^3. The crystal structure consists of $[BiBr_6]^{3-}$ octahedra, protonated 2-amino-5-picolinium cations $(C_6H_9N_2)^+$, and free water molecules. These building units are interconnected through a network of hydrogen bonds and π π⋯π π interactions, resulting in a stable zero-dimensional (0D) architecture (Fig. 1).

The asymmetric unit of $(C_6H_9N_2)_3[BiBr_6]\cdot H_2O$, depicted in Fig. 2, comprises two crystallographically independent bismuth(III) ions. The first ion, Bi1, occupies a special position on a twofold axis (Wyckoff site 4e). It is coordinated to four bromide ions: two located at general positions (Br1 and Br2) and two situated on special positions on the same twofold axis (Br3 and Br4). Its octahedral coordination sphere is completed by two additional bromide ions generated by the symmetry code ($1 - x, y, 1/2 - z$).

The second bismuth(III) ion, Bi2, occupies a special position on an inversion center (Wyckoff site 4c) and is directly bonded to three bromide ions (Br5, Br6, Br7) located at general positions. Three more bromide ions (Br5′, Br6′, Br7′) generated by an inversion center complete the coordination sphere around Bi2.

As shown in Fig. 1, the hexabromidobismuthate(III) ions, $[BiBr_6]^{3-}$, are arranged in such a way that they form inorganic layers parallel to the (1 0 −1) plane and are isolated from one another with a minimum intermetallic Bi–Bi distance of

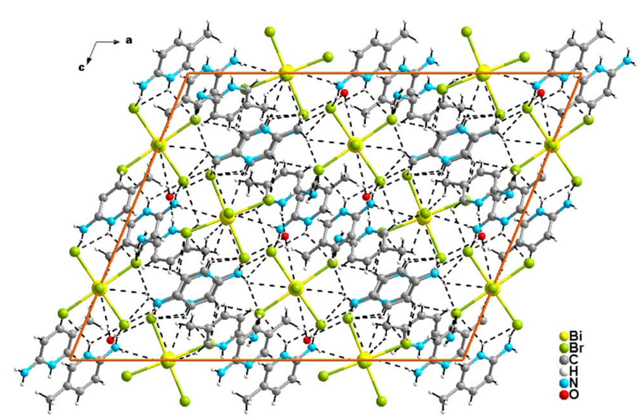

Fig. 1 Projection of the structure of $(C_6H_9N_2)_3[BiBr_6]\cdot H_2O$ along the crystallographic b-axis.

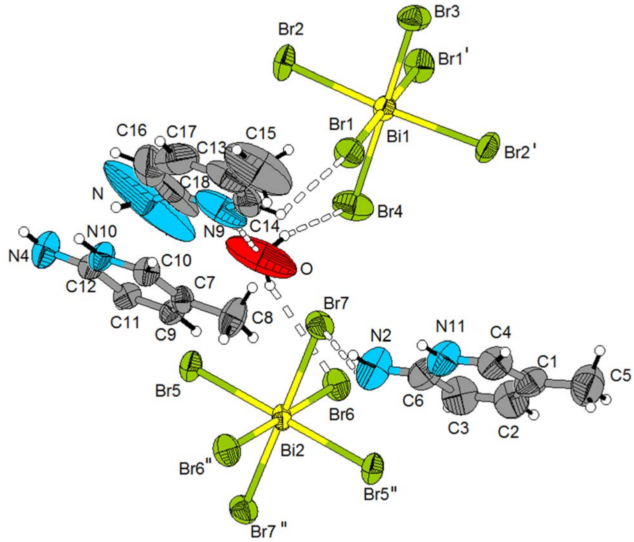

Fig. 2 The asymmetric unit of $(C_6H_9N_2)_3[BiBr_6]\cdot H_2O$. Hydrogen bonds are represented by dashed lines (symmetry codes: ^{I} $1-x, y, 1/2-z$: ^{II} $3/2-x, 1/2-y, 1-z$).

8.7694(8) Å. Within the $[BiBr_6]^{3-}$ anions, the Bi–Br bond distances range from 2.7537(10) to 2.9841(11) Å for $Bi1Br_6$, and from 2.8474(7) to 2.8559(7) Å for $Bi2Br_6$ while the *cis*-Br–Bi–Br angles vary between 88.043(17) and 91.957(17)° and between 86.69(2) and 93.31(2)° for $Bi1Br_6$ and $Bi2Br_6$, respectively (Table 2). These geometric features are consistent with those observed in other compounds containing $BiBr_6$ octahedra.[30–32] The Bi–Br bond distance in this study, 2.8512(7) Å, is longer than the Sb–Br bond distance found in $(C_6H_9N_2)_2[SbBr_4]Br$, where Sb–Br distances range from 2.5698(5) to 2.709(4) Å, with a mean value of 2.6817(4) Å.[29]

This difference is expected, as the Bi^{3+} ion is more voluminous than the Sb^{3+} ions ($r_{Bi^{3+}} = 1.2$ Å and $r_{Sb^{3+}} = 0.76$ Å). Considering the geometrical characteristics of the $[BiBr_6]^{3-}$ anions in our compound, the calculated average Baur indices (DI) were obtained using the following equation:[33]

$$\mathrm{DI(Bi-Br)} = \sum_{i=1}^{n_1} \frac{|d_i - d_m|}{n_1 d_m}; \quad (2)$$

$$\mathrm{DI(Br-Bi-Br)} = \sum_{i=1}^{n_2} \frac{|a_i - a_m|}{n_2 a_m} \quad (3)$$

where d represents the Bi–Br distance, a is the Br–Bi–Br angle, m denotes the average value, and $n_1 = 6$ and $n_2 = 12$ for an octahedral environment.

The calculated distortion indices, DI (Bi1–Br) = 0.0156 and DI (Bi2–Br) = 0.0011, along with DI (Br–Bi–Br) values of 0.012 and 0.025 for $Bi1Br_6$ and $Bi2Br_6$, respectively, indicate that the coordination geometry of bismuth is a slightly distorted octahedron. This distortion is due to the environment surrounding the $[BiBr_6]^{3-}$ octahedra and particularly the intermolecular hydrogen bonds formed with the organic cations and water molecules.

The negative charges of the anionic $[BiBr_6]^{3-}$ octahedra are compensated by the protonated amines, $(C_6H_9N_2)^+$, which are arranged to form organic cationic layers parallel to the (1 0 −1) plane (Fig. 1). The crystal structure of the title compound can thus be described as an alternating pattern of organic and inorganic layers, which are directed towards the [1 0 1] direction (Fig. 1). The bond distances and angles characteristic of the protonated amines, listed in Table 2, are consistent with those found in the other compounds containing the same organic cation.[29,34–37] Unlike the anionic octahedra, which are isolated from one another, the organic cations are connected through $\pi\cdots\pi$ interactions in a parallel-displaced configuration of the amine aromatic rings.[38,39] Indeed, the shortest distance between the planes of two adjacent protonated amine aromatic rings is 3.6005(3) Å (Fig. S1). The $\pi\cdots\pi$ interactions in the title compound are slightly weaker than those found in the previously reported antimony-based compound, $(C_6H_9N_2)_2[SbBr_4]Br$, where the shortest centroid-to-centroid distance between aromatic rings is 3.4422(2) Å.[29]

The asymmetric unit of $(C_6H_9N_2)_3[BiBr_6]\cdot H_2O$ contains only one free water molecule, which plays a crucial role in the cohesion of the crystal structure. Specifically, it facilitates connections between the anionic octahedra and the cationic organic entities through hydrogen bonds. This water molecule acts as a donor in Ow–H⋯Br hydrogen bonds and as an acceptor in N–H⋯Ow interactions (Fig. 3(a)). Notably, the anionic and cationic entities are directly linked *via* N–H⋯Br hydrogen bonds and weak non-covalent C–H⋯Br interactions. Within these intermolecular hydrogen bonds, distances are as follows: N⋯Br distances range from 3.324(11) to 3.926(6) Å, C⋯Br distances are comprised between 3.695(6) and 3.881(6) Å, O⋯Br distances vary between 3.476(7) and 3.827(11) Å, and the N⋯O distance measures 2.834(11) Å. The D–H⋯A angles fall within the 121.1–171.3° (Table S2).

3.2. Optical properties

Fig. 4 displays the absorption spectra of the synthesized compound $(C_6H_9N_2)_3[BiBr_6]\cdot H_2O$. The absorption spectrum exhibits a characteristic profile commonly observed in bismuth-based materials.[31,40–42] Five distinct absorption bands are identified, centered at 233, 256, 296, 373, and 420 nm. In the UV region, three prominent bands appear at 233, 256, and 296 nm,

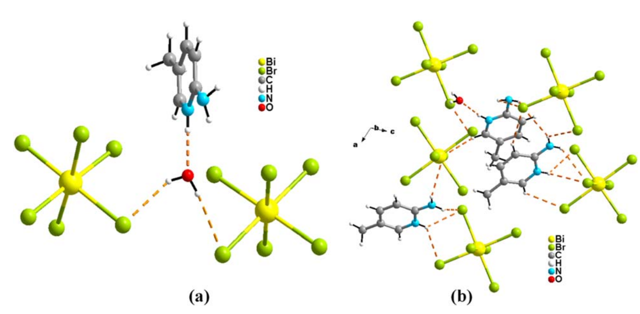

Fig. 3 Hydrogen bonds established by (a) the water molecule and (b) the protonated amine in $(C_6H_9N_2)_3[BiBr_6]\cdot H_2O$.

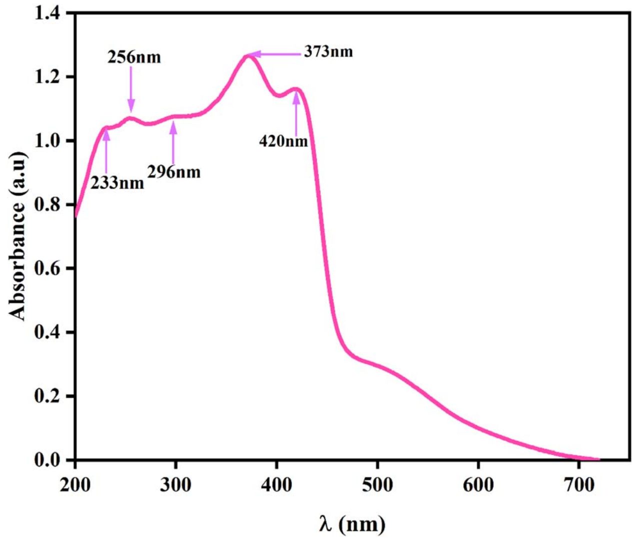

Fig. 4 UV-vis absorption spectra of $(C_6H_9N_2)_3[BiBr_6]\cdot H_2O$ compound.

which are attributed to $\pi \rightarrow \pi^*$ and $n \rightarrow \pi^*$ electronic transitions associated with the pyridine rings.[43] The broader bands observed around 373 and 420 nm are ascribed either to metal-centered (MC) transitions[40] or to ligand-to-metal charge transfer (LMCT) transitions.[41,42]

In semiconductors and insulating materials, the energy band gap (E_g) is the smallest amount of energy required to excite an electron from the valence band to the conduction band through photon absorption. This gap significantly influences the optical properties of the material, including its absorption characteristics, color, and transparency. As a result, E_g is an important parameter across various fields, such as solar energy conversion, light emission technologies, and laser systems.

According to the method proposed by Marotti, Henríque, and their collaborators,[44,45] the optical bandgap energy (E_g) can be estimated from the reflectance spectrum ($R(\lambda)$) by identifying the maximum of the function$(1/R(\lambda))(dR(\lambda)/d\lambda)$. As shown in Fig. S2, this function exhibits a prominent peak at 439 nm for the studied material. Using the standard relation $E(\text{eV}) = 1240/\lambda(\text{nm})$,[46] the corresponding band gap energy is calculated to be 2.82 eV. This value falls within the typical range for semiconductors (0.5–5 eV) and is comparable to that of the related compound $(C_9H_{12}N_4)_2[BiBr_6]\cdot Cl\cdot 4H_2O$ (3.483 eV),[10] although it is lower than that of $[C_8H_{12}N]_3BiCl_6$ (4.42 eV).[47]

To determine whether the optical band transition mode of the studied materials is direct or indirect, Tauc's law was applied,[48] as expressed by:

$$(F(R)h\nu)^{1/n} = C(h\nu - E_g) \quad (4)$$

where, h represents Plank's constant ($\sim 6.6 \times 10^{-34}$ J), $F_{KM}(R(\lambda)) = \dfrac{(1 - R(\lambda))^2}{2R(\lambda)}$ is the Kubelka Munk function $h\nu$ denotes the energy of the incident photon (in eV), and C is the band edge sharpness constant. The exponent n indicates the nature of the optical transition: $n = 2$ corresponds to an allowed direct transition, while $n = 1/2$ corresponds to an allowed indirect band gap.[49]

The optical band gap is determined using the Tauc plot method, where $[F(R(\lambda))h\nu]^2$ (direct transitions) and $[F(R(\lambda))h\nu]^2$ (indirect transitions) are plotted against photon energy. The band gap was estimated by extrapolating the linear portion of the Tauc plot to the energy axis, where $[F(R)h\nu]^n = 0$ (Fig. 5). For $(C_6H_9N_2)_3[BiBr_6]\cdot H_2O$, this analysis yields an indirect band gap of 2.87 eV and a direct band gap of 2.81 eV, consistent with the reflectance-derived value of 2.82 eV (Fig. S2).

Although both types of transitions were identified, the direct transition dominates the optical behavior of the compound. This conclusion is substantiated by its exact correspondence with the reflectance-derived E_g (2.82 eV, Fig. S2) and the characteristic steep absorption onset at 440 nm, hallmarks of direct-gap semiconductors. The marginally higher indirect gap may originate from phonon-assisted processes but remains spectroscopically secondary. Consequently, all subsequent optoelectronic interpretations reference the direct transition at 2.81 eV.

3.3. Electrical properties

3.3.1. Complex impedance results. Fig. 6 illustrates the evolution of the Nyquist curves measured between 318 K and 363 K. These curves provide insight into the resistive (real part Z') and reactive (imaginary part Z'') components of the synthesized compound $(C_6H_9N_2)_3[BiBr_6]\cdot H_2O$. The impedance plots display a single, depressed semicircle, which results from the overlapping contributions of two distinct semicircular arcs typically associated with grain and grain boundary effects. Notably, there is no observable contribution from the electrode-sample interface. As illustrated in Fig. 6, the diameter of the semicircle decreases with increasing temperature, indicating an enhancement of DC conductivity. To analyze these contributions in more detail, the Maxwell–Wagner equivalent circuit model[50] was employed. This model consists of multiple resistor–capacitor (R–C) elements arranged in parallel, allowing the differentiation between grain and grain boundary responses

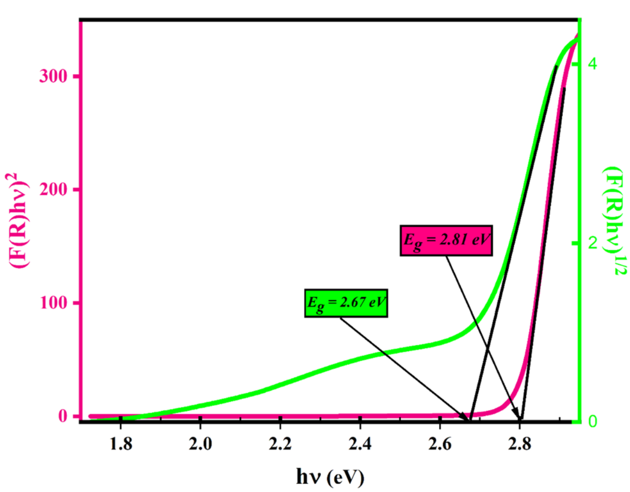

Fig. 5 Tauc plot for $(C_6H_9N_2)_3[BiBr_6]\cdot H_2O$ compound.

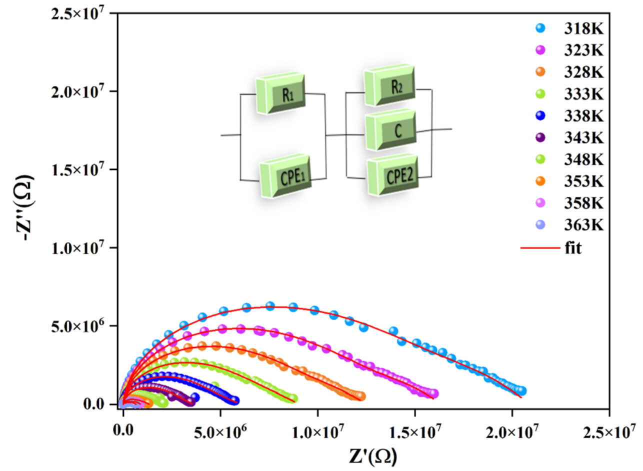

Fig. 6 Variation of the Nyquist plots measured at different temperatures, 318–363 K, with the proposed equivalent circuits for the investigated compound.

within the single semicircle. The corresponding circuit, shown in the inset of Fig. 6, includes a parallel R_1–CPE_1 element representing the grain response, connected in series with an R_2–C–CPE_2 element that models the grain boundary response. The constant phase element (CPE) accounts for the non-ideal capacitive behavior typically attributed to dipolar relaxation phenomena. The parameters obtained for the circuit components are outlined in Table S3.

Fig. 7 presents the frequency dependence of the real part of the complex impedance (Z') at various temperatures. The data reveal three distinct regions, each characterized by different conduction behaviors influenced by both frequency and temperature:

• Low-frequency region: at low frequencies, Z' exhibits a strong temperature dependence, while remaining largely independent of frequency. A plateau is often observed, suggesting that the response is dominated by grain boundary effects. This behavior is typically attributed to charge carrier accumulation at grain boundary interfaces, leading to interfacial polarization and pronounced low-frequency impedance dispersion.

• Intermediate-frequency region ($\sim 10^2$ to 10^5 Hz): in this region, both frequency and temperature significantly influence the Z' values. Z' decreases with increasing frequency and also diminishes with rising temperature, indicating enhanced charge carrier mobility. This behavior corresponds to an increase in AC conductivity, which becomes more prominent with thermal activation.

• High-frequency region: at higher frequencies, the Z' values exhibit convergence across all temperatures, reflecting reduced impedance contributions. This convergence may be associated with the release of space charges and a corresponding reduction in interfacial polarization effects. Additionally, the temperature-induced lowering of potential barriers facilitates charge transport, resulting in a further decrease in AC resistance.[51]

The imaginary component of the complex impedance ($-Z''$) as a function of frequency at various temperatures is presented in Fig. 8. The spectra exhibit well-defined peaks corresponding to the maximum of $-Z''$ (denoted as $-Z''_{\rm max}$) at specific frequencies ($\omega_{\rm max}$), which are associated with the material's electrical relaxation processes. These peaks occur within the dispersion region of the real part of impedance (Z'). As the temperature increases, the relaxation peaks shift toward higher frequencies, indicating that the relaxation mechanism is thermally activated.[52] The observed peaks are asymmetric and broadened over the entire temperature range, which is characteristic of a non-Debye type relaxation behavior, implying the presence of a distribution of relaxation times. Furthermore, the convergence of $-Z''$ at high frequencies suggests the possible contribution of space charge relaxation effects.[53] This behavior of $-Z''$ at both low and high frequencies is consistent with

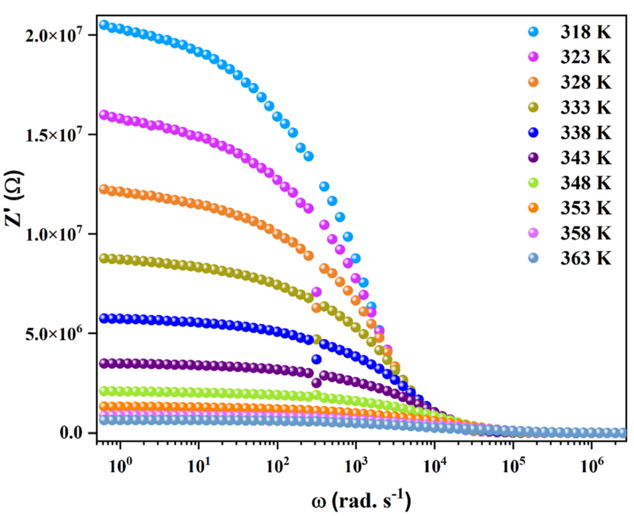

Fig. 7 Frequency dependence of Z' at various temperatures of$(C_6H_9N_2)_3[BiBr_6]\cdot H_2O$ compound.

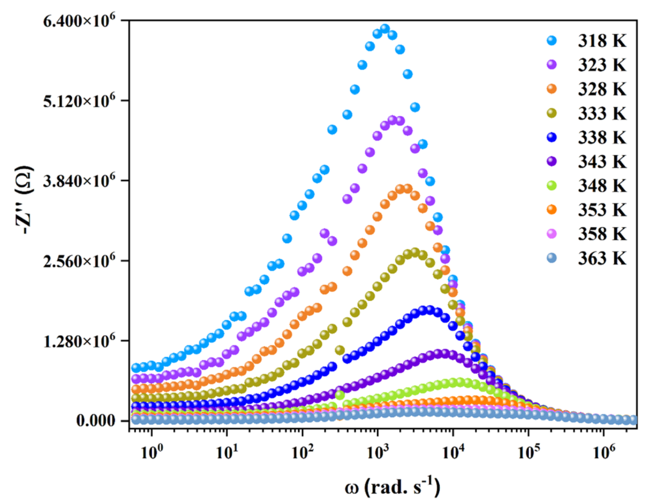

Fig. 8 Frequency dependence of $-Z''$ at various temperatures of$(C_6H_9N_2)_3[BiBr_6]\cdot H_2O$ compound.

previously reported results for similar organic–inorganic hybrid systems.[54–56]

3.3.2. AC electrical conductivity and conduction mechanism analysis. The AC conductivity analysis was performed to gain deeper insight into how the material's electrical behavior varies with frequency. The dependence of AC conductivity on frequency is a powerful method for characterizing the nature of charge transport mechanisms.[57] Fig. 9 illustrates how σ_{ac} evolves with frequency across a range of temperatures. The compound under investigation exhibits conductivity values between 10^{-8} and 10^{-6} S cm^{-1}, confirming its semiconducting nature.

As depicted in Fig. 9, the conductivity spectra display two distinct regions. In the low-frequency range (1–10^3 rad s^{-1}), σ_{ac} remains almost constant, implying minimal frequency dependence. This plateau suggests a thermally activated transport process, likely associated with DC conductivity, which becomes more pronounced with increasing temperature. At higher frequencies, the conductivity increases, forming a dispersive region. This behavior is attributed to localized charge carriers within the grains acquiring enough energy to overcome potential barriers over short distances. The conductivity follows Jonscher's universal power law:[34]

$$\sigma_{ac} = \sigma_{dc} + A\omega^s \tag{5}$$

where σ_{dc} denotes the DC conductivity evident at low frequencies, A is a temperature-dependent pre-factor, and the exponent s (with values between 0 and 1) reflects the degree of interaction between the mobile charge carriers and their surrounding lattice environment.

Furthermore, the temperature dependence of the frequency exponent s provides valuable insights into the dominant charge transport mechanism within the material.[58–61] By fitting the experimental AC conductivity data to Jonscher's power law, important trends emerge, particularly about how s varies with temperature, as depicted in Fig. 10. The results show a clear decrease in the value of s with increasing temperature, a behavior that is consistent with the correlated barrier hopping (CBH) conduction model.[62]

$$s(T) = 1 - \frac{6k_BT}{W_M + k_BT\ln(\omega\tau_0)} \tag{6}$$

When the condition $W_M \gg k_BT\ln(\omega\tau_0)$ is satisfied, this equation simplifies to:

$$s(T) = 1 - \frac{6k_BT}{W_M} \tag{7}$$

Fig. 10 presents as well the linear fitting of the $(1 - s)$ parameter as a function of temperature for the investigated material. From the slope of this fit, the maximum barrier height (W_M) is estimated to be approximately 0.32 eV. Notably, the exponent s remains consistently below unity across the entire temperature range, which reinforces the interpretation that charge transport occurs *via* localized hopping processes. This behavior aligns well with the theoretical framework proposed by Funke, which describes charge carrier dynamics in disordered materials through thermally activated hopping between energetically favorable sites.

3.3.3. DC conductivity study. Fig. 11 shows a linear (affine) plot of $\ln(\sigma_{dc} \times T)$ *versus* $1000/T$, exhibiting behavior consistent with the Arrhenius equation:

$$\sigma_{dc}T = A\exp\left(-\frac{E_a}{k_BT}\right) \tag{8}$$

where E_a is the activation energy, A is the pre-exponential factor, k_B is the Boltzmann constant, and T is the absolute temperature. The plot reveals two distinct linear regions corresponding to different activation energies: $E_{a_1} = 0.51$ eV in the 318–333 K range, and $E_{a_2} = 0.96$ eV between 333–363 K. The higher-temperature activation energy (E_{a_2}) is attributed to bromide ion (Br^-) hopping.[55] This transition suggests a change in the dominant conduction mechanism as temperature increases.

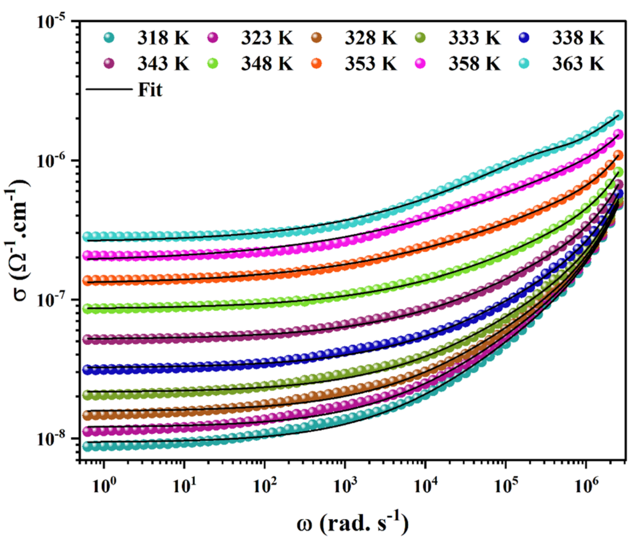

Fig. 9 Frequency dependence of ac conductivity for different temperatures.

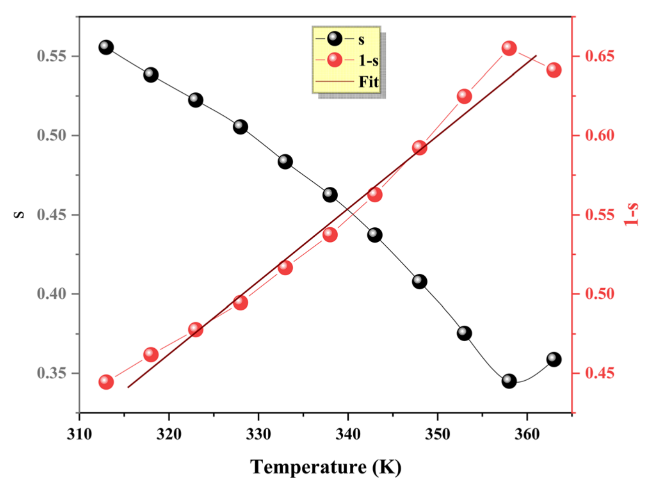

Fig. 10 Thermal variation of exponent (s) and $(1 - s)$.

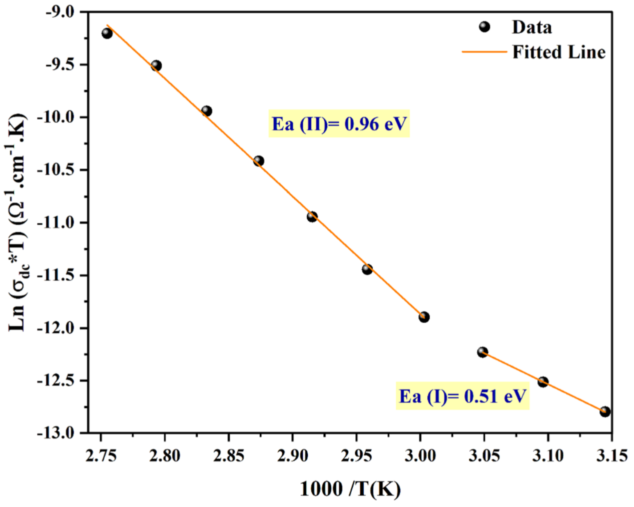

Fig. 11 Temperature dependence of $\mathrm{Ln}(\sigma^*_{dc}T)$ of $(C_6H_9N_2)_3[BiBr_6]\cdot H_2O$ compound.

3.3.4. **Complex modulus analysis.** The complex electrical modulus formalism is widely regarded as a valuable alternative method for investigating the electrical behavior of materials. This approach offers deeper insight into various electrical phenomena, making it particularly effective for analyzing conductivity relaxation dynamics and minimizing the influence of electrode polarization effects.[63] Mathematically, the complex modulus is defined by the following expression:

$$M = j\omega C_0 Z = M' + jM'' \tag{9}$$

The temperature-dependent evolution of the real part of the electrical modulus (M') across the studied frequency range is illustrated in Fig. 12. At low frequencies, M' remains close to zero for all temperatures, indicating a negligible contribution from electrode polarization. Conversely, at higher frequencies, M' increases and eventually tends toward a saturation value M_∞. This behavior reflects relaxation phenomena and charge conduction associated with localized, short-range carrier mobility.

Fig. 13 shows the frequency-dependent behavior of the imaginary part of the electrical modulus (M'') at various temperatures. The results reveal a broad, asymmetric relaxation peak. At low frequencies, the M'' values approach zero, indicating a negligible contribution from electrode effects.[64] Each curve displays a single asymmetric peak, and the position of the peak maximum (ω_{max}) shifts toward higher frequencies as temperature increases, highlighting the thermally activated nature of the relaxation process.

In the frequency region below ω_{max}, charge carriers are likely able to move over long distances. In contrast, in the region beyond ω_{max}, they become confined within potential wells, limiting their mobility to shorter distances.[20] The imaginary component $M''(\omega)$ was modeled using the following relation:

$$M'' = \frac{M''_{max}}{(1-\beta) + \frac{\beta}{(1+\beta)}\left[\beta\left(\frac{\omega_{max}}{\omega}\right) + \left(\frac{\omega}{\omega_{max}}\right)^{\beta}\right]} \tag{10}$$

In this expression, ω_{max} and M''_{max} represent the frequency and magnitude of the peak in the M'' spectrum, respectively, while β is the well-known Kohlrausch exponent. The spectral shape for each temperature was characterized using β, initially estimated from the full width at half maximum (FWHM) of the M'' peak. This β parameter was then fine-tuned to optimize the fit to eqn (10) at each temperature.

The best fits of $M''(\omega)$ across the temperature range are displayed in Fig. 13. The corresponding β values are summarized in Table S4, clearly showing a temperature-dependent trend. All values fall within the interval $0 < \beta < 1$, indicating a non-Debye type relaxation and reflecting the strong coupling between mobile ions involved in the conduction mechanism.

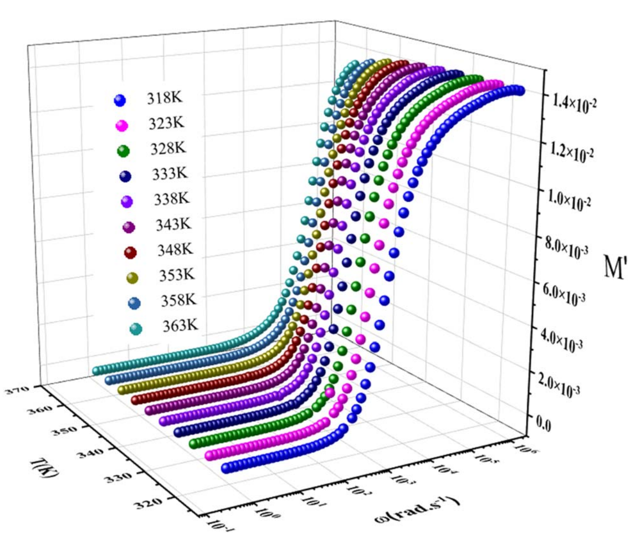

Fig. 12 Frequency-dependent M' at different temperatures for $((C_6H_9N_2)_3[BiBr_6]\cdot H_2O$.

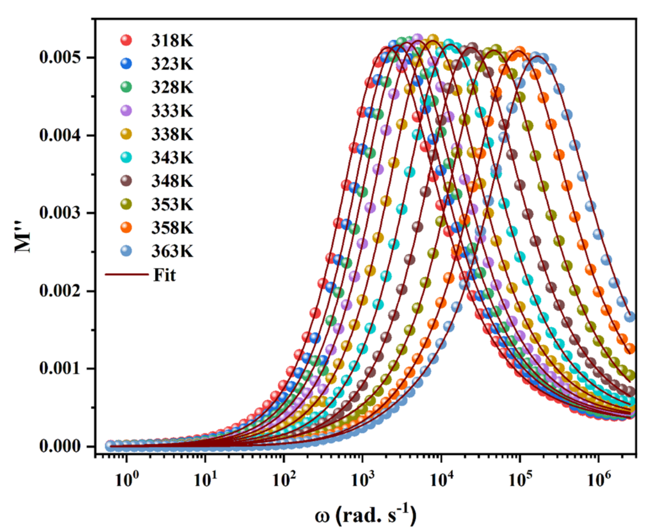

Fig. 13 Frequency-dependent M'' at different temperatures for $(C_6H_9N_2)_3[BiBr_6]\cdot H_2O$ compound.

4 Dielectric study

The use of the complex permittivity formalism has proven to be an effective method for uncovering key chemical and physical aspects related to the electrical and dielectric behavior of materials. This approach is mathematically described by:[65–67]

$$\varepsilon(\omega) = \varepsilon'(\omega) + j\varepsilon''(\omega) \tag{11}$$

where ε' and ε'' represent the real and imaginary parts of the dielectric constant, respectively.

Fig. 14(a) and (b) illustrate the frequency dependence of ε' and ε'' at various temperatures ranging from 318 K to 363 K. From the data, it is evident that the real part ε' increases significantly at low frequencies with rising temperature, followed by a sharp decline beyond approximately 10^2 Hz. This behavior confirms that $\varepsilon'(\omega)$ is influenced by bound charge polarization, which plays a role in the material's ability to store electric energy.

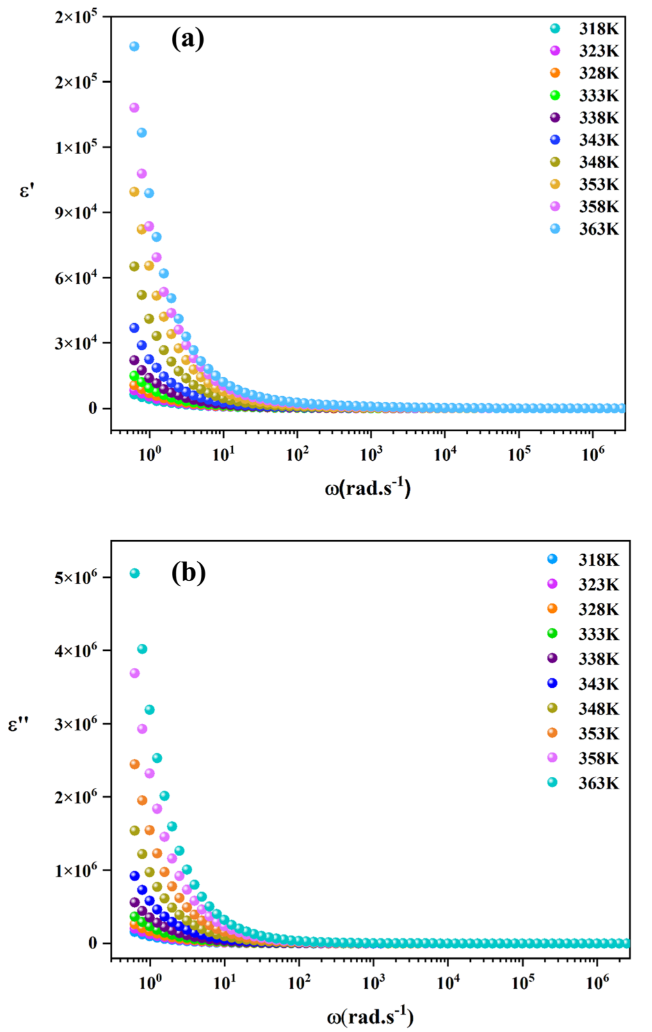

Fig. 14 Frequency-dependent (a) real part (ε') and (b) imaginary part (ε'') of the dielectric permittivity.

Similarly, the imaginary part ε'' also increases with temperature, which reflects the presence of a broad distribution of relaxation times in the studied compound. The imaginary component ε'' provides insight into the energy dissipation processes. In general, dielectric response is governed by four types of polarization mechanisms: interfacial, dipolar, electronic, and ionic. At low frequencies, ε' is mainly dominated by interfacial and dipolar polarization, indicating a deviation from ideal Debye relaxation behavior. The pronounced decline of ε' at higher frequencies is attributed to the gradual loss of space charges, which otherwise enhance the dielectric response.

The dielectric measurements reveal that the investigated compound exhibits a remarkably high real permittivity (ε'), reaching up to 10^5 at 363 K. To ensure that this exceptionally elevated dielectric constant is not significantly affected by electrode polarization, a detailed analysis was conducted using the electric modulus formalism. As illustrated in Fig. 14 and 15, both the real (M') and imaginary (M'') components of the complex modulus approach zero at low frequencies across the entire studied temperature range (318–363 K), indicating negligible electrode polarization effects. This behavior suggests that the observed dielectric response is dominated by intrinsic material properties rather than interfacial electrode contributions. Additionally, impedance spectroscopy data, reinforced by equivalent circuit modeling (inset of Fig. 6), further support the absence of significant electrode-related artifacts, as no low-frequency semicircle typically associated with electrode effects was detected.

To contextualize this result, Table 3 presents a comparison between the dielectric constant of $(C_6H_9N_2)_3[BiBr_6]\ H_2O$ and those of similar bismuth-based or hybrid compounds. The permittivity observed in our compound significantly surpasses that of other reported materials, such as $[C_{13}H_{16}N_2]_5(BiCl_6)3Cl$ ($\varepsilon' \approx 10^4$),[20] (pyrrolidinium)$_3[Bi_2I_9]$ ($\varepsilon' \approx 500$),[68] and conventional semiconductors like the B4ATCZ crystal ($\varepsilon' \approx 26.2$).[69] This elevated dielectric response is likely attributed to intrinsic structural features, including interfacial polarization at grain

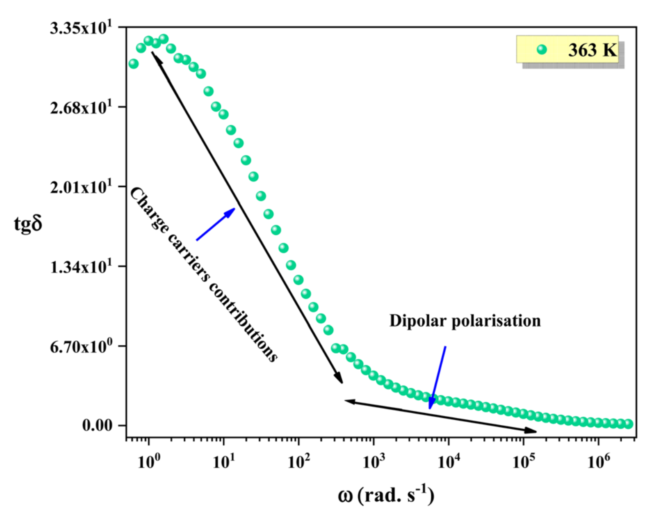

Fig. 15 tg(δ) *vs.* angular frequency spectra of $(C_6H_9N_2)_3[BiBr_6]\ H_2O$.

Table 3 Dielectric constant comparison

Compound	Dielectric constant	Reference
$[C_{13}H_{16}N_2]_5(BiCl_6)3Cl$	10^4	20
B4ATCZ	26.2	69
$(Pyrrolidinium)_3[Bi_2I_9]$	45	68
$SrBi_4Ti_4O_{15}$	70–165	70
$Ba_{0.85}Ca_{0.15}Ti_{0.9}Zr_{0.1}O_3$ (BCZT)	5.3×10^3–9.6×10^3	71
$CaCu_3Ti_4O_{12}$	10^3–10^4	72
$(C_6H_9N_2)_3[BiBr_6]\ H_2O$	10^5	This work

boundaries, strong dipolar interactions, and thermally activated charge hopping mechanisms. Collectively, these characteristics point to the promising potential of $(C_6H_9N_2)_3[BiBr_6]$ H_2O for advanced dielectric applications, such as capacitive energy storage, microelectronics, and photonic technologies.

The variation of the dielectric loss tangent, tg(δ), as a function of frequency at 363 K is displayed in Fig. 15. The dielectric loss factor, tg(δ), is defined by the relation:

$$\mathrm{tg}(\delta) = \frac{\varepsilon''}{\varepsilon'} \tag{12}$$

At lower frequencies, tg(δ) exhibits a prominent peak before gradually decreasing with increasing frequency. This behavior reflects the presence of two distinct relaxation processes in the material. The first peak appears in the low-frequency range (1–10^3 rad s^{-1}) and is attributed to space charge polarization. The second peak, located in the mid-frequency domain (10^3–10^6 rad s^{-1}), is associated with dipolar polarization. These observations indicate the contribution of multiple polarization mechanisms, including electronic, ionic, orientational, and space charge effects, most notably in the low-frequency region.[73,74]

As frequency increases, the material's resistivity decreases, enabling easier movement of charge carriers. Consequently, the energy required for their motion diminishes, which explains the reduction in dielectric loss observed at higher frequencies. Furthermore, Fig. 15 demonstrates that tg(δ) values for the investigated compound remain relatively low, ranging approximately from 0.01 to 35. This low dielectric loss is particularly beneficial for optoelectronic device applications.[75–77]

Given these properties, the $(C_6H_9N_2)_3[BiBr_6]$. H_2O compound shows great potential for use in optoelectronic systems. It is also important to note that the dielectric loss tangent, tg(δ), plays a crucial role in determining energy efficiency and thermal stability of materials. Higher values of tg(δ) generally correspond to greater energy dissipation and heat generation. In contrast, controlled or minimal dielectric losses, as seen in capacitors, can enhance device efficiency. Thus, tg(δ) significantly influences the performance of technologies related to electronics, telecommunications, and energy storage.

5 Conclusion

In summary, the novel hybrid compound $(C_6H_9N_2)_3[BiBr_6]\cdot H_2O$ has been successfully synthesized and structurally characterized, revealing a zero-dimensional monoclinic structure stabilized by hydrogen bonding and π–π interactions. Optical measurements confirm its semiconducting nature, with a direct band gap of approximately 2.81 eV. Impedance spectroscopy demonstrates a non-Debye relaxation with distinct grain and grain boundary contributions, well modeled by a dual equivalent circuit.

The DC conductivity exhibits Arrhenius-type temperature dependence, with two distinct activation energies, which reflect a change in the conduction mechanism. AC conductivity analysis, along with the temperature-dependent behavior of the frequency exponent s, supports the correlated barrier hopping (CBH) model as the primary conduction process. Additionally, the compound demonstrates significant dielectric permittivity, indicating a strong response to external electric fields, an essential feature for energy storage and conversion applications.

Overall, these results underscore the potential of $(C_6H_9N_2)_3[BiBr_6]\cdot H_2O$ as a promising candidate for future development in optoelectronic devices and advanced energy-related technologies.

Author contributions

Rima Altalib: writing – original draft, validation, software, methodology, investigation. Imen Ibrahmi: writing – original draft, validation, software, methodology, investigation. Arafet Ghoudi: writing – original draft, visualization, formal analysis. Sami Znaidia: formal analysis, validation, writing review. Walid Rekik: writing – review & editing, visualization, validation. Jerome Lhoste: writing – review & editing, validation, investigation, formal analysis. Abderrazek Oueslati: writing – review & editing, visualization, validation, investigation, formal analysis, data curation.

Conflicts of interest

The authors declare that they have no known competing financial interests or personal relationships that could have appeared to influence the work reported in this paper.

Data availability

Additional data can be provided by the authors upon reasonable request.

CCDC 2371583 contains the supplementary crystallographic data for this paper.[78]

All data supporting the findings of this study are available within the article and its SI. See DOI: https://doi.org/10.1039/d5ra04097c.

Acknowledgements

This work is financially supported by the Ministry of Higher Education and Scientific Research of Tunisia.

References

1 S. Hermi, M. G. Althobaiti, A. A. Alotaibi, A. H. Almarri, W. Fujita, F. Lefebvre, *et al.*, Synthesis, Crystal Structure, DFT Theoretical Calculationand Physico-Chemical Characterization of a New Complex Material (C6H8Cl2N2)2 [Cd3Cl10]·6H2O, *Crystals*, 2021, **11**(5), 553.

2 L. Zhang, J. Wang, J. Wu, S. Mo, F. Long, Z. Zou, *et al.*, Crystal structure, optical behavior and electrical conduction of the new organic–inorganic compound CH3NH3CdI3, *J. Mater. Sci.: Mater. Electron.*, 2018, **29**(12), 9821–9828.

3 I. Garoui, M. Mallek, F. N. Almutairi, W. Rekik and A. Oueslati, Synthesis, Structural characterization and complex impedance analysis of a novel organic-inorganic hybrid compound based on Mercury (II) chloride, *J. Mol. Struct.*, 2024, **1315**, 138881.

4 X. Lu, L. Zhang, Y. Tong and Z. Y. Cheng, BST-P(VDF-CTFE) nanocomposite films with high dielectric constant, low dielectric loss, and high energy-storage density, *Composites, Part B*, 2019, **168**, 34–43.

5 Y. Wang, T. Guo, J. Yin, Z. Tian, Y. Ma, Z. Liu, *et al.*, Controlled Deposition of Zinc-Metal Anodes via Selectively Polarized Ferroelectric Polymers, *Adv. Mater.*, 2022, **34**(4), 2106937.

6 D. Fredj, C. B. Hassen, S. Elleuch, H. Feki, N. C. Boudjada, T. Mhiri, *et al.*, Structural, vibrational and optical properties of a new organic–inorganic material: (C5H8N3)2 [BiCl5], *Mater. Res. Bull.*, 2017, **85**, 23–29.

7 W. Trigui and F. Hlel, Ferroelectric properties and Raman spectroscopy of the [(C4H9)4N]3Bi2Cl9 compound, *RSC Adv.*, 2019, **9**(42), 24291–24298.

8 D. Lencer, M. Salinga and M. Wuttig, Design Rules for Phase-Change Materials in Data Storage Applications, *Adv. Mater.*, 2011, **23**(18), 2030–2058.

9 P. F. Li, W. Q. Liao, Y. Y. Tang, H. Y. Ye, Y. Zhang and R. G. Xiong, Unprecedented Ferroelectric–Antiferroelectric–Paraelectric Phase Transitions Discovered in an Organic–Inorganic Hybrid Perovskite, *J. Am. Chem. Soc.*, 2017, **139**(25), 8752–8757.

10 A. Alibi, M. Ben Hassen, N. Elleuch, S. Mnif, F. Chabchoub and M. Boujelbene, Non-centrosymmetric bismuth-based (C9H12N4)2[BiBr6]·Cl·4H2O hybrid material:Detailed investigation of optical properties, and antibacterial study, *Opt. Mater.*, 2025, **159**, 116585.

11 Z. Aloui, C. Ounelli, M. Essid, F. Nicolò, G. Bella, A. Santoro, *et al.*, Synthesis, crystal structure, vibrational studies, optical properties and DFT calculation of a new Bi(III) halide complex: (C9H14N3)4[Bi2Cl11][BiCl6].4H2O, *J. Solid State Chem.*, 2022, **316**, 123572.

12 A. Ben Ahmed, H. Feki and Y. Abid, Synthesis, crystal structure, vibrational spectroscopy, optical properties and theoretical studies of a new organic–inorganic hybrid material: [((CH3)2NH2)+]6·[(BiBr6)3−]2, *Spectrochim. Acta, Part A*, 2014, **133**, 357–364.

13 S. Chkoundali, I. Garoui, W. Trigui and A. Oueslati, Crystal structure, Hirshfeld surface analysis, conduction mechanism and electrical modulus study of the new organic–inorganic compound [C8H10NO]2HgBr 4, *RSC Adv.*, 2024, **14**(13), 8971–8980.

14 Y. Gao, X. Dong and Y. Liu, Recent Progress of Layered Perovskite Solar Cells Incorporating Aromatic Spacers, *Nano-Micro Lett.*, 2023, **15**(1), 169.

15 E. Mahal, S. Charan Mandal and B. Pathak, Understanding the role of spacer cation in 2D layered halide perovskites to achieve stable perovskite solar cells, *Mater. Adv.*, 2022, **3**(5), 2464–2474.

16 S. A. Sharber, W. J. Mullin and S. W. Thomas, Bridging the Void: Halogen Bonding and Aromatic Interactions to Program Luminescence and Electronic Properties of π-Conjugated Materials in the Solid State, *Chem. Mater.*, 2021, **33**(17), 6640–6661.

17 E. Bouaziz, O. Kammoun, A. Slassi, D. Cornil, J. Lhoste, S. Auguste, *et al.*, A supramolecular non centrosymmetric 2,6-diaminopyridinium perchlorate salt: Crystal structure and optoelectronic DFT study, *J. Mol. Struct.*, 2022, **1267**, 133561.

18 J. A. Bis and M. J. Zaworotko, The 2-Aminopyridinium-carboxylate Supramolecular Heterosynthon: A Robust Motif for Generation of Multiple-Component Crystals, *Cryst. Growth Des.*, 2005, **5**(3), 1169–1179.

19 A. Fatima, M. Singh, K. M. Abualnaja, K. Althubeiti, S. Muthu, N. Siddiqui, *et al.*, Experimental Spectroscopic, Structural (Monomer and Dimer), Molecular Docking, Molecular Dynamics Simulation and Hirshfeld Surface Analysis of 2-Amino-6-Methylpyridine, *Polycyclic Aromat. Compd.*, 2023, **43**(5), 3910–3940.

20 K. Kahouli, A. B. J. Kharrat, K. Khirouni and S. Chaabouni, Electrical conduction mechanism and dielectric properties of the [C13H16N2]5(BiCl6)3Cl hybrid compound, *Appl. Phys. A*, 2023, **129**(6), 431.

21 N. Elfaleh, S. Karoui and S. Kamoun, Ionic conductivities and dielectric analysis of (C6H20N3)BiI6·H2O compound, *Indian J. Phys.*, 2022, **96**(8), 2337–2344.

22 L. K. Wu, Y. Feng, Z. J. Wang, L. H. Li, Z. B. Hu, H. Y. Ye, *et al.*, Metal-dependent structural phase transition and dielectric response in two organic–inorganic hybrids of [C4H10N]2[SbCl5] and [C4H10N]3[BiCl6], *Inorg. Chem. Commun.*, 2022, **142**, 109641.

23 M. Hamdi, S. Karoui, A. Oueslati, S. Kamoun and F. Hlel, Synthesis, crystal structure and dielectric properties of the new organic -inorganic hybrid compound [C6H10N2]7 [Bi2Cl11]2.4[Cl], *J. Mol. Struct.*, 2018, **1154**, 516–523.

24 Bruker, *SAINT*, Bruker AXS Inc., Madison, Wisconsin, USA, 2002.

25 G. M. Sheldrick, SADABS. Bruker AXS Inc., Madison, Wisconsin, USA, *Acta Crystallogr., Sect. E: Struct. Rep. Online*, 2002, 1600–5368.

26 G. M. Sheldrick, Crystal structure refinement with SHELXL, *Acta Crystallogr., Sect. C*, 2015, **71**(1), 3–8.

27 L. J. Farrugia, WinGX suite for small-molecule single-crystal crystallography, *J. Appl. Crystallogr.*, 1999, **32**(4), 837–838.

28 K. Brandenburg and H. Putz, *Crystal Impact GbR*, Bonn, Germany, 2012, This article is licensed under a Creative Commons Attribution 3.

29 I. Chaabane, W. Rekik, M. Zaghrioui, J. Lhoste, A. Oueslati and M. Gargouri, Synthesis, crystal structure, and ionic conductivity of a new organic–inorganic bromides (C6H9N2)2[SbBr4]Br, *Ionics*, 2024, **30**(9), 5827–5844.

30 N. Elfaleh and S. Kamoun, Crystal structure, vibrational and optical properties of N-(3-ammoniumpropyl)-1,3 diammoniumpropane hexabromobismuthate monohydrate: [C6H20N3]BiBr6 H2O, *J. Mol. Struct.*, 2014, **1075**, 479–485.

31 M. Essid, Z. Aloui, V. Ferretti, F. Lefebvre and C. B. Nasr, Crystal structure, vibrational and optical properties of a new Bi(III) halide complex: [C6H16N2]5Bi2Br10(BiBr6) 2·2H2O, *Inorg. Chim. Acta*, 2017, **466**, 235–242.

32 I. Walha, D. Díaz-García, S. Gómez-Ruiz, M. Abdelhedi and F. Zouari, Unveiling the Synthesis, Hirshfeld Surface Insights, and Interesting Photocatalytic Ability of [C7H8N3] 6(BiBr6)2·3H2O, *J. Mol. Struct.*, 2024, **1309**, 138184.

33 W. H. Baur, The geometry of polyhedral distortions. Predictive relationships for the phosphate group, *Acta Crystallogr., Sect. B*, 1974, **30**(5), 1195–1215.

34 A. Ghoudi, K. B. Brahim, H. Ghalla, J. Lhoste, S. Auguste, K. Khirouni, *et al.*, Crystal structure and optical characterization of a new hybrid compound, C 6 H 9 N 2 FeCl 4 , with large dielectric constants for field-effect transistors, *RSC Adv.*, 2023, **13**(19), 12844–12862.

35 I. Ben-Gharbia, R. Kefi, C. Ben-Nasr and A. Durif, Structure and characterization of a new inorganic-organic hybrid complex of Zn(II) with 2-amino-4-methylpyridine, *Rev. Roum. Chim.*, 2008, **53**, 169–175.

36 A. S. Albrecht, C. P. Landee and M. M. Turnbull, Structure of bis(2-amino-5-methylpyridinium) tetrachlorozincate at 298 and 150 K, *J. Chem. Crystallogr.*, 2003, **33**(4), 269–276.

37 I. Chaabane, W. Rekik, H. Ghalla, M. Zaghrioui, J. Lhoste and A. Oueslati, Crystal structure, optical characterization, conduction and relaxation mechanisms of a new hybrid compound (C6H9N2)2[Sb2Cl8], *RSC Adv.*, 2024, **14**(5), 3588–3598.

38 C. Janiak, A critical account on π–π stacking in metal complexes with aromatic nitrogen-containing ligands, *J. Chem. Soc., Dalton Trans.*, 2000, (21), 3885–3896.

39 N. J. Singh, S. K. Min, D. Y. Kim and K. S. Kim, Comprehensive Energy Analysis for Various Types of π-Interaction, *J. Chem. Theory Comput.*, 2009, **5**(3), 515–529.

40 K. Oldenburg, A. Vogler, I. Mikó and O. Horváth, Photoredox decomposition of tin(II), lead(II), antimony(III) and bismuth(III) iodide complexes in solution, *Inorg. Chim. Acta*, 1996, **248**(1), 107–110.

41 A. Vogler, A. Paukner and H. Kunkely, Photochemistry of coordination compounds of the main group metals, *Coord. Chem. Rev.*, 1990, **97**, 285–297.

42 A. Vogler and H. Nikol, Photochemistry and photophysics of coordination compounds of the main group metals, *Pure Appl. Chem.*, 1992, **64**(9), 1311–1317.

43 A. Ghoudi, I. Chaabane, R. Naouari, A. Aydi, A. Oueslati, E. Dhahri, *et al.*, Optical and electric properties of the organic-inorganic hybrid bis(2-amino-5-picolinium) Tetrachlorocobaltate(II) [(C6H9N2)2CoCl4], *Inorg. Chem. Commun.*, 2024, **168**, 112925.

44 R. E. Marotti, D. N. Guerra, C. Bello, G. Machado and E. A. Dalchiele, Bandgap energy tuning of electrochemically grown ZnO thin films by thickness and electrodeposition potential, *Sol. Energy Mater. Sol. Cells*, 2004, **82**(1), 85–103.

45 R. Henríquez, P. Grez, E. Muñoz, H. Gómez, J. A. Badán, R. E. Marotti, *et al.*, Optical properties of CdSe and CdO thin films electrochemically prepared, *Thin Solid Films*, 2010, **518**(7), 1774–1778.

46 K. B. Brahim, M. B. Gzaiel, A. Oueslati, K. Khirouni, M. Gargouri, G. Corbel, *et al.*, Organic–inorganic interactions revealed by Raman spectroscopy during reversible phase transitions in semiconducting [(C2H5)4N] FeCl 4, *RSC Adv.*, 2021, **11**(30), 18651–18660.

47 M. Essid, Z. Aloui, V. Ferretti, S. Abid, F. Lefebvre, M. Rzaigui, *et al.*, Crystal structure, Hirshfeld surface and spectroscopic studies of the noncentrosymmetric Bi(III) halide complex: [C8H12N]3BiCl6, *Inorg. Chim. Acta*, 2017, **457**, 122–129.

48 S. K. Gagandeep, B. S. Lark and H. S. Sahota, Attenuation Measurements in Solutions of Some Carbohydrates, *Nucl. Sci. Eng.*, 2000, **134**(2), 208–217.

49 H. Elgahami, A. Ghoudi, B. Azaza, H. Khmissi, A. Sanchez-Coronilla, A. Oueslati, *et al.*, Mercury (II) compound with a quaternary phosphonium: X-ray structure, Hirshfeld surface analysis, optical band gap, and dielectric properties, *Ionics*, 2025, **31**(1), 1095–1110.

50 J. Liu, C. g. Duan, W. N. Mei, R. W. Smith and J. R. Hardy, Dielectric properties and Maxwell-Wagner relaxation of compounds ACu3Ti4O12 (A=Ca, Bi2/3, Y2/3, La2/3), *J. Appl. Phys.*, 2005, **98**(9), 093703.

51 H. Nejeh, A. Oueslati and W. Rekik, A new organic–inorganic chloride (H3N–(CH2)6–NH3)[SnCl6]: Crystal structure, thermal analysis, vibrational study, and electrical properties, *Polyhedron*, 2024, **264**, 117250.

52 A. Ray, A. Roy, S. De, S. Chatterjee and S. Das, Frequency and temperature dependent dielectric properties of TiO2-V2O5 nanocomposites, *J. Appl. Phys.*, 2018, **123**(10), 104102.

53 D. K. Pradhan, P. Misra, V. S. Puli, S. Sahoo, D. K. Pradhan and R. S. Katiyar, Studies on structural, dielectric, and transport properties of Ni0.65Zn0.35Fe2O4, *J. Appl. Phys.*, 2014, **115**(24), 243904.

54 I. Kammoun, M. Belhouchet, A. B. Ahmed, J. Lhoste and M. Gargouri, Investigation of structural, optical and electrical conductivity of a new organic inorganic bromide: [C 12 H 17 N 2] 2 ZnBr 4, *RSC Adv.*, 2023, **13**(12), 8034–8042.

55 A. Ghoudi, S. Auguste, J. Lhoste, W. Rekik, H. Ghalla, K. Khirouni, *et al.*, Crystal Structure and Spectroscopic Characterization of a New Hybrid Compound, (C12H17N2) 2[CdBr4], for Energy Storage Applications, *ACS Omega*, 2024, **9**(26), 28339–28353.

56 N. Elfaleh, H. Chouaib, S. Kamoun and M. P. F. Graça, AC conductivity analysis and dielectric relaxation behavior of (C6H20N3)BiBr6.H2O, *J. Phys. Org. Chem.*, 2015, **28**(11), 674–680.

57 H. Khachroum, M. Krimi, M. S. M. Abdelbaky, S. García-Granda and M. Dammak, A comprehensive study of crystal structure, UV–visible study, electric-dielectric properties of a recently developed Hybrid Material [(C6H5N2)2ZnCl4], *Mater. Res. Bull.*, 2024, **179**, 112978.

58 G. E. Pike, ac Conductivity of Scandium Oxide and a New Hopping Model for Conductivity, *Phys. Rev. B*, 1972, **6**(4), 1572–1580.

59 A. Ghosh and D. Chakravorty, AC conduction in semiconducting CuO-Bi2O3-P2O5 glasses, *J. Phys.: Condens. Matter*, 1990, **2**(24), 5365.

60 X. L. Cleac'h, Lois de variations et ordre de grandeur de la conductivité alternative des chalcogénures massifs non cristallins, *J. Phys.*, 1979, **40**(4), 417–428.

61 P. Yadav and A. Sharma, Temperature and frequency dependence of AC conductivity of new quaternary Se-Te-Bi-Pb chalcogenide glasses, *AIP Conf. Proc.*, 2016, **1728**(1), 020189.

62 S. R. Elliott, A. c. conduction in amorphous chalcogenide and pnictide semiconductors, *Adv. Phys.*, 1987, **36**(2), 135–217.

63 A. V. Sarode and A. C. Kumbharkhane, Dielectric relaxation study of poly(ethylene glycols) using TDR technique, *J. Mol. Liq.*, 2011, **164**(3), 226–232.

64 B. Louati, K. Guidara and M. Gargouri, Dielectric and ac ionic conductivity investigations in the monetite, *J. Alloys Compd.*, 2009, **472**(1), 347–351.

65 Y. S. Altındal, E. Erbilen Tanrıkulu and M. Ulusoy, Dielectric properties of MS diodes with Ag:ZnO doped PVP interfacial layer depending on voltage and frequency, *Mater. Chem. Phys.*, 2023, **303**, 127788.

66 I. M. Hodge and C. A. Angell, Electrical relaxation in amorphous protonic conductors, *J. Chem. Phys.*, 1977, **67**(4), 1647–1658.

67 H. J. Schütt, A new phenomenological description of the electrical relaxation in ionic conductors, *Solid State Ionics*, 1994, **72**, 86–88.

68 M. Rowińska, A. Piecha-Bisiorek, W. Medycki, P. Durlak, R. Jakubas and A. Gagor, Structural, Electric and Dynamic Properties of (Pyrrolidinium)3[Bi2I9] and (Pyrrolidinium)3[Sb2I9]: New Lead-Free, Organic–Inorganic Hybrids with Narrow Band Gaps, *Molecules*, 2023, **28**(9), 3894.

69 M. Suriya, M. Manimaran, B. M. Boaz and K. S. Murugesan, Investigation on the optical, spectral, electrical, mechanical, and laser damage threshold studies of bis (4-acetylanilinium) tetrachloridozincate (B4ATCZ) crystal, *J. Mater. Sci.: Mater. Electron.*, 2021, **32**(9), 11393–11417.

70 H. C. Ling, M. F. Yan and W. W. Rhodes, High dielectric constant and small temperature coefficient bismuth-based dielectric compositions, *J. Mater. Res.*, 1990, **5**(8), 1752–1762.

71 Z. Hanani, D. Mezzane, M. Amjoud, S. Fourcade, A. G. Razumnaya, I. A. Luk'yanchuk, *et al.*, Enhancement of dielectric properties of lead-free BCZT ferroelectric ceramics by grain size engineering, *Superlattices Microstruct.*, 2019, **127**, 109–117.

72 B. A. Bender and M. J. Pan, The effect of processing on the giant dielectric properties of CaCu3Ti4O12, *Mater. Sci. Eng., B*, 2005, **117**(3), 339–347.

73 S. A. Yerişkin, G. E. Demir and İ. Yücedag, On the Frequency-Voltage Dependence Profile of Complex Dielectric, Complex Electric Modulus and Electrical Conductivity in Al/ZnO/p-GaAs Type Structure at Room Temperature, *J. Nanoelectron. Optoelectron.*, 2019, **14**(8), 1126–1132.

74 A. Tataroglu, H. Durmuş, A. F. Vahid, B. Avar and Ş. Altındal, High-temperature sensitivity complex dielectric/electric modulus, loss tangent, and AC conductivity in Au/(S:DLC)/p-Si (MIS) structures, *J. Mater. Sci.: Mater. Electron.*, 2024, **35**(3), 227.

75 A. Prajapati and G. Shalev, Omnidirectional and Wideband Absorption of Solar Radiation with Light Funnel Arrays Incorporated with Quasi-Nanolenses, *ACS Appl. Energy Mater.*, 2022, **5**(5), 5331–5339.

76 A. Prajapati and G. Shalev, Arrays of Fresnel Nanosystems for Enhanced Photovoltaic Performance, *ACS Omega*, 2023, **8**(26), 23365–23372.

77 F. Xie, H. Tang, X. Zhao, M. Li, L. Li and J. Cheng, Thin-Film Solar Cells using a Selenized Silver Antimony Sulfide Absorber Prepared by Spray Pyrolysis Deposition, *Phys. Status Solidi RRL*, 2021, **15**(12), 2000514.

78 R. Altalib, I. Ibrahmi, A. Ghoudi, S. Znaidia, W. Rekik, J. Lhoste and A. Oueslati, CCDC 2371583: Experimental Crystal Structure Determination, 2025, DOI: 10.5517/ccdc.csd.cc2kltpp.

